Annual Variations in the Near-Earth Solar Wind

Mathew J. Owens[1] · Mike Lockwood[1] · Luke A. Barnard[1] · Stephanie L. Yardley[1] ·
Heli Hietala[2] · Adrian T. LaMoury[3] · Laura Vuorinen[4]

Abstract

Earth's orbit and rotation produces systematic variations in geomagnetic activity, most notably via the changing orientation of the dayside magnetospheric magnetic field with respect to the heliospheric magnetic field (HMF). Aside from these geometric effects, it is generally assumed that the solar wind in near-Earth is uniformly sampled. But systematic changes in the intrinsic solar wind conditions in near-Earth space could arise due to the annual variations in Earth heliocentric distance and heliographic latitude. In this study, we use 24 years of *Advanced Composition Explorer* data to investigate the annual variations in the scalar properties of the solar wind, namely the solar wind proton density, the radial solar wind speed and the HMF intensity. All parameters do show some degree of systematic annual variation, with amplitudes of around 10 to 20%. For HMF intensity, the variation is in phase with the Earth's heliocentric distance variation, and scaling observations for distance largely explains the observed variation. For proton density and solar wind speed, however, the phase of the annual variation is inconsistent with Earth's heliocentric distance. Instead, we attribute the variations in speed and density to Earth's heliographic latitude variation and systematic sampling of higher speed solar wind at higher latitudes. Indeed, these annual variations are most strongly ordered at solar minimum. Conversely, combining scalar solar wind parameters to produce estimates of dynamic pressure and potential power input to the magnetosphere results in solar maximum exhibiting a greater annual variation, with an amplitude of around 40%. This suggests Earth's position in the heliosphere makes a significant contribution to annual variations in space weather, in addition to the already well-studied geometric effects.

1. Introduction

Variability in the near-Earth solar wind can disturb the terrestrial magnetosphere. When the orientation of the heliospheric magnetic field (HMF) is anti-parallel to that at the dayside

---

✉ M.J. Owens
   m.j.owens@reading.ac.uk

1   Department of Meteorology, University of Reading, Earley Gate, PO Box 243, Reading RG6 6BB,
    UK

2   Department of Physics and Astronomy, Queen Mary University of London, Mile End Road,
    London E1 4NS, UK

3   The Blackett Laboratory, Imperial College London, Exhibition Road, London SW7 2AZ, UK

4   Department of Physics and Astronomy, University of Turku, Turku, Finland

magnetopause, magnetic reconnection can lead to efficient energization of the terrestrial system (Dungey, 1961). As the Earth's magnetic dipole is (on average) broadly aligned with the solar rotation axis, the ambient Parker spiral HMF (Parker, 1958) and the dayside magnetopause magnetic field are (on average) closer to orthogonal than antiparallel. Additional processes that give rise to southward magnetic field, B_S, in the terrestrial frame are needed to drive the most intense geomagnetic activity (Lockwood et al., 2016). Geomagnetic storms – periods of intense, long-duration disturbance to the magnetosphere – are driven by the arrival of a coronal mass ejection (CME) in near-Earth space (Gosling, 1993), as the internal CME magnetic field can contain a strong, sustained B_S component.

Moderate B_S can also be generated by the ambient HMF due to Earth's axial tilt and orbit around the Sun (see Lockwood et al., 2020b; Cliver, Kamide, and Ling, 2002, for more complete overviews of this subject). There are three such geometric effects:

- The Russell–McPherron (RM) effect (Russell and McPherron, 1973) arises from tilt of the Earth's magnetic dipole relative to the Earth's rotation axis, and the annual variation of the Earth's rotation axis relative to the solar equator (Cortie, 1912, 1913). As the angle between the nominal Parker-spiral HMF and the dayside magnetopause magnetic field varies, this gives rise to peaks in geomagnetic activity at the equinoxes, in March and September, as well as systematic diurnal variations. The RM effect depends strongly on the azimuthal or Y-component of the HMF in the solar frame (B_Y) and gives a strong peak at about 10 UT at the September equinox for HMF $B_Y > 0$ and a strong peak around 22 UT at the March equinox for HMF $B_Y > 0$ (Zhao and Zong, 2012). However, because B_Y polarities are present with almost equal occurrence probabilities and because the response of geomagnetic activity is not just a half-wave rectification of B_S, the RM effect for all data combined is rather weak, despite the fact it is very strong for each of the two B_Y polarities individually (Lockwood et al., 2020b; Lockwood and Milan, 2023).
- The equinoctial effect also arises from the inclination of the Earth's magnetic axis, but as it tilts towards or away from the Sun (McIntosh and Feather, 1959). This also maximises geomagnetic activity around the equinoxes, but with a different diurnal pattern than the RM effect.
- The axial effect arises from the inclination of Earth's orbit relative to the solar equator (Cortie, 1912, 1913). As with the previous two effects, this results in geomagnetic activity peaks at the equinoxes, but as it does not involve Earth rotation, it does not produce any diurnal variation. While not strictly a geometric effect, but when Earth is at high heliographic latitude, it can lead to preferential sampling of the HMF polarity associated with the polar field (Rosenberg and Coleman, 1969).

Note that these geometric effects are important for the mean level of geomagnetic activity and the core of the distribution of geomagnetic responses, but not of great importance for the large-event tail of the distribution: the long-lived southward HMF in the magnetospheric frame that generates major storms is also found in the southward component of the HMF in solar frames (Lockwood et al., 2016). Hence large geomagnetic storms are generated by persistent deflection of the HMF toward southward (in both the Earth and solar frames) associated with CMEs and not by large B_Y HMF and tilt of the Earth's dipole (i.e. the Russell–McPherron effect).

Geometric effects and their annual variations have long been acknowledged as important to geomagnetic activity (e.g. Lockwood et al., 2019, and references therein). But the annual variation in the scalar properties of the solar wind – namely the solar wind density, speed, and HMF intensity – are not as well appreciated. It is often implicitly assumed that the near-Earth solar wind is uniformly sampled throughout the year. A number of studies have hinted that this may not be a valid assumption.

Due to the slightly elliptical orbit, Earth is approximately 3.5% closer to the Sun in northern-hemisphere winter than in summer. Due to the inverse-square variation of density with distance, this might be expected to give around 7% change in solar wind plasma density, on average. This effect has been noted in the near-Earth solar wind (Lockwood et al., 2020a). However, as will be demonstrated in this article, the reality may be more complex, due to the heliolatitude and distance variations of Earth being intrinsically coupled. Earth's variation in heliolatitude by ± 7.25 degrees over the year can lead to systematic sampling of different solar wind types. Murayama (1974) and Orlando et al. (1993) have suggested that preferential sampling of fast wind when Earth is at high heliographic latitudes may contribute to the geomagnetic activity variation ascribed to the RM effect. This study aims to understand and quantify the annual variations in near-Earth solar wind properties.

2. Near-Earth Solar Wind Data

Solar wind observations are provided by the *Advanced Composition Explorer* (ACE) magnetic field and solar wind instruments (McComas et al., 1998; Smith et al., 1998). ACE was selected for its orbital position, which does not vary significantly with respect to Earth throughout the entire mission lifetime, simplifying the interpretation of the results. The data are available at 64-second resolution, which is subsequently averaged up to 1 hour. We primarily consider the scalar quantities of solar wind proton number density, n_P, heliospheric magnetic-field intensity, $|B|$, and radial solar wind speed, V_r. We do not investigate the magnetic-field orientation factors, as they primarily couple to geomagnetic activity through the daily and annual variations of the orientation of the Earth's magnetosphere, which have been well studied elsewhere (see Lockwood et al., 2020b; Cliver, Kamide, and Ling, 2002).

In order to investigate the effect of removing solar wind intervals known to result from the interplanetary coronal mass ejections (ICMEs), we use a list of manually identified ICMEs (Richardson and Cane, 2010). Both ICMEs and preceding sheath are removed for the 'No ICMEs' dataset, using the observed boundaries. Removing an additional day of data prior to the start of the sheath and after the ICME trailing edge does not significantly change the results presented here.

Before investigating the annual variations in solar wind parameters, it is instructive to understand the interrelation between the solar wind parameters themselves. The solar wind has long been known to have two primary states: 'Fast' wind tends to have lower plasma density and magnetic-field intensity than 'slow' wind, also referred to as streamer belt wind (e.g. McComas et al., 2003; Ebert et al., 2009; Bloch et al., 2020; Owens, 2020). Fast wind is also referred to as coronal hole wind and thus is primarily encountered at high latitudes at solar minimum when polar coronal holes dominate. In the ecliptic plane at Earth orbital distance, it is rare to encounter fast wind that has not been somewhat slowed and compressed by interaction with the more dominant slow wind (McComas et al., 2003).

Figure 1 shows median properties of the solar wind over the full ACE dataset, at 1-hour resolution. Data have been split into 25 equal-width bins and the error on the median is computed as the 95% confidence interval from a bootstrapping method (McGill, Tukey, and Larsen, 1978), wherein the original distribution is repeatedly sampled with replacement 1000 times. Varying bin sizes does not qualitatively affect these results. The scaling of solar wind speed, density, and magnetic-field intensity to account for the small radial distance variation of ACE, shown in red, is described in Section 3. It has very little effect on the trends discussed here. Figure 1a shows the expected result that high speed wind is less dense than low speed wind. However, in the ecliptic plane at Earth orbital distance, the distinct fast and

Figure 1 The interdependence of solar wind parameters from 1-hour resolution ACE observations over the period 1998 to 2023. Lines show median values, error bars are 95% confidence intervals on the medians. Black and blue lines show the observed values over the whole dataset with and without ICMEs, respectively. Red lines show the data scaled to 215 $r_\odot$ (1 AU), as described in Section 3. (a) Solar wind proton density, n_P, as a function of solar wind radial speed, V_R. (b) Heliospheric magnetic-field intensity, $|B|$, as a function of V_R. (c) $|B|$ as a function of n_P.
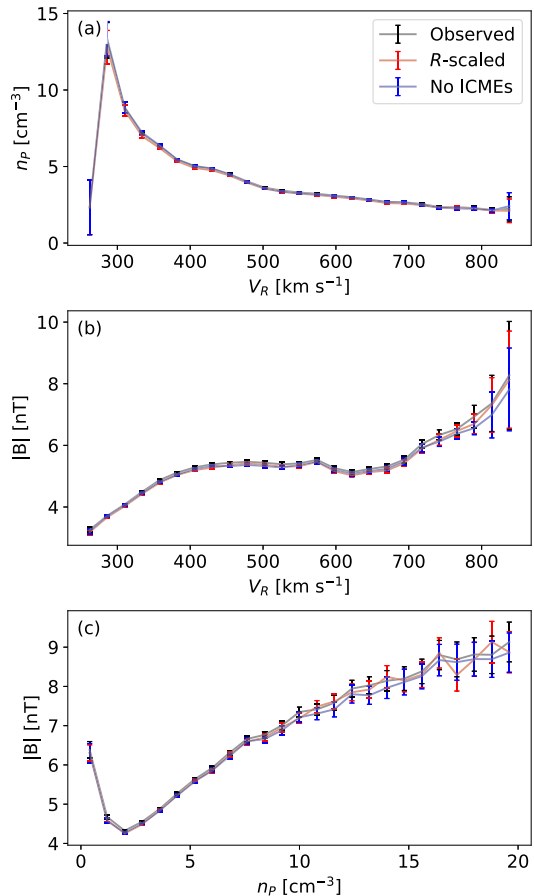
slow wind populations are not readily discernible, and the relation appears to be continuous. Figure 1c shows that, in general, $|B|$ also increases with n_P, consistent with the typical fast and slow wind properties (Ebert et al., 2009). Though, again, there is more of a continuous variation than two distinct populations. Note also that for very low n_P (< 2 cm^{-3}), $|B|$ increases. This is not the result of identifiable ICME material. Figure 1b shows a weak increase in $|B|$ with V_R. This runs counter to the fast and slow wind paradigms (Ebert et al., 2009) and the results shown in Figures 1a and 1c. This apparent contradiction is likely the result of using a single value – the median – to describe a distribution, which contains contributions from multiple populations within the solar wind. Indeed, this can be seen to some degree in the relation between n_P and $|B|$ (Figure 1c): High $|B|$ populations exist for both very high and very low n_P. As these broad interrelations are presented here only as context for the annual variations discussed below, we do not investigate these features further in this study.

    In order to investigate solar cycle variations, we use the daily sunspot number (SSN), provided by the Sunspot Index and Long-term Solar Observations (SILSO) activity of the Solar Influences Data-analysis Center (SIDC) (Clette and Lefèvre, 2016), and available from https://www.sidc.be/silso/. While we use version 2.0 of the SILSO record, the 1998 to 2022 interval considered in this study is not subject to any of the calibration issues or correc-

tions that are necessary for the early data (Clette et al., 2023). As the solar wind structure is expected to be primarily a function of the solar cycle phase (e.g. Owens, 2020), we also construct a solar activity index (SAI, Owens et al., 2022), aimed at characterising the progression of the solar cycle independent of the variation in sunspot cycle amplitude:

$$SAI(t) = \frac{SSN_{13}(t)}{\max\left[SSN_{13}(t - 5.5\text{yr} : t + 5.5\text{yr})\right]}, \tag{1}$$

where $SSN_{13}(t)$ is the 13-month smoothed sunspot number centred on time t. It is computed as a rolling average at daily intervals. This is normalised by the maximum SSN_{13} value in an 11-year window centred on t. Thus, by construction, SAI has a minimum possible value of 0 and reaches a maximum value of 1 in every solar cycle. To select out periods of solar minimum and maximum, we use SAI thresholds of 0.25 and 0.67, respectively. These values are somewhat arbitrary, but give approximately equal duration intervals of minimum and maximum. The results presented here are not qualitatively sensitive to the choice of these thresholds.

3. Spaceship Earth

Figure 2 shows the orbital characteristics of Earth and ACE. In Figure 2a it can be seen that while ACE is in a halo orbit about the L1 point, the heliographic latitudes, θ, of ACE and Earth are essentially identical. Figure 2b shows that ACE, near the L1 point, is typically

Figure 2 Time series of Earth and ACE orbital characteristics over 1998 – 2022. (a) The heliographic latitude of ACE (red) and Earth (black). (b) The heliocentric distance, R, from the Sun. (c) The ratio of the ACE-Earth distance, R_{AE}, to the Earth-Sun distance, R_{ES}. (d) The 13-month smoothed sunspot number, scaled by a factor 1/200 (black) and the solar activity index, SAI (red). The red dashed lines show the SAI thresholds used to define solar minimum and solar maximum.
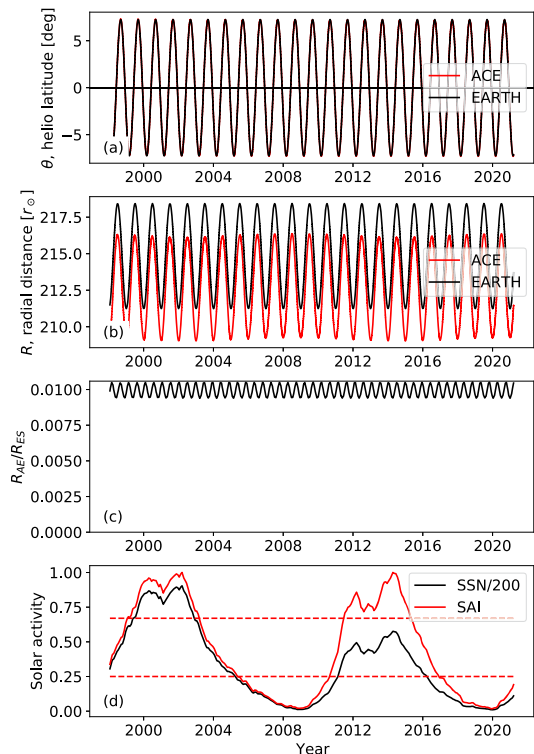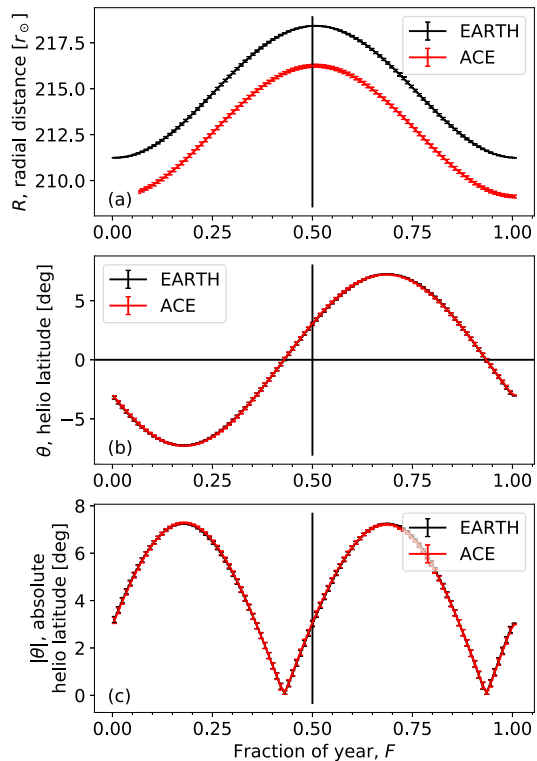
Figure 3 The median orbital variations as a function of fraction of the year, F. Error bars are one standard error on the median. ACE is shown in red, Earth in black. (a) The heliocentric radial distance, R. (b) The heliographic latitude, θ. (c) The absolute heliographic latitude, $|\theta|$. For reference, $F = 0.5$ is shown as a solid vertical black line.

1-2 solar radii ($r_\odot$) closer to the Sun than Earth and Figure 2c shows that the ACE-Earth distance, R_{AE} is an almost constant fraction (0.01) of the Earth-Sun distance, R_{ES}. Thus, ACE data can be treated as representative of near-Earth solar wind over the whole period considered. Finally, Figure 2d shows the 13-month smoothed SSN and SAI variations over this interval. There are two solar cycles of observations from which we select out solar minimum and maximum intervals that comprise around a third of the dataset each.

Figure 3 shows the median annual variations of ACE and Earth orbital parameters as a function of fraction of calendar year, F. Figure 3a shows that perihelion occurs at $F = 0.01$ (early January), while aphelion is at $F = 0.51$ (early July). Figures 3b and c show that Earth is at the helioequator at $F = 0.43$ (early June) and $F = 0.94$ (mid-December). Thus, Earth reaches maximum $|\theta|$ at $F = 0.17$ (early March) and $F = 0.69$ (early September).

The blue, black and red lines in Figure 4 show how observed solar wind parameters vary with heliocentric distance and latitude. Black and blue lines show, respectively, the observed values over all data and with ICMEs removed. There are no particularly obvious trends, though see further discussion below. However, as shown in Figure 3, R and θ are closely interconnected, particularly with the largest and smallest R values being associated with both high and low $|\theta|$. This makes it difficult to directly disentangle these effects on the solar wind encountered by Earth.

One means to separate the R and θ contributions is to scale parameters for the expected R variation. By conservation of mass, the proton number density, n_P, in a spherically expanding solar wind should fall off as $1/R^2$. This ignores any dynamics – compression or rarefaction – that may occur within the few solar radii of variation in ACE heliocentric distance. The value of R at ACE (and at Earth) varies by around 7 $r_\odot$ over the year, which is
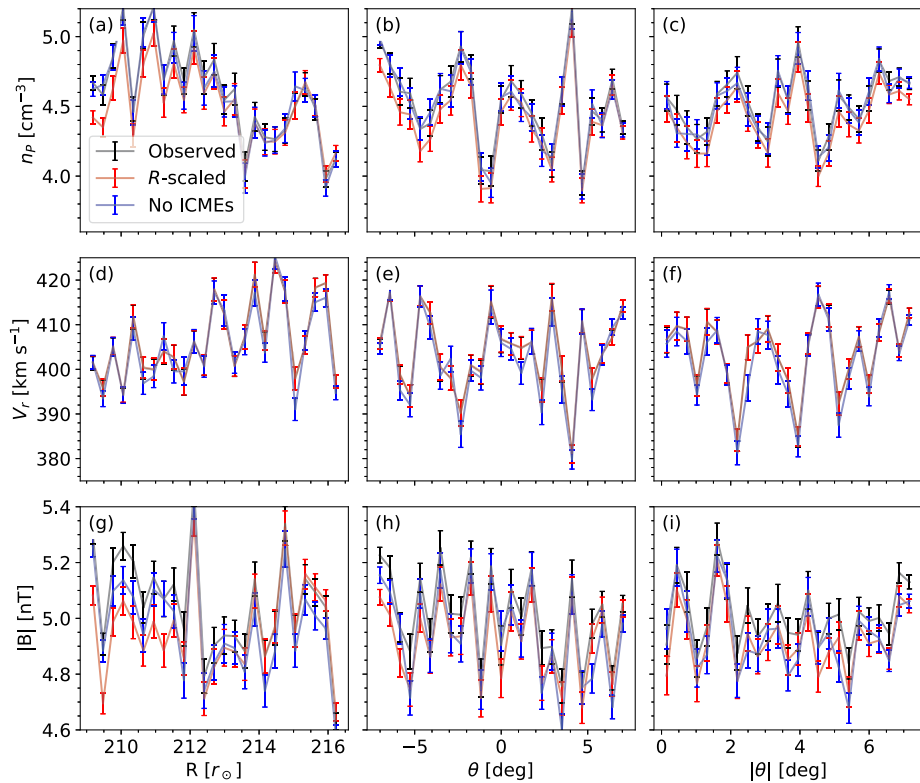
Figure 4 Variations of near-Earth solar wind conditions with Earth orbital parameters, namely heliocentric distance (left), heliographic latitude (middle), and absolute latitude (right). Lines show median values, error bars are 95% confidence interval on the median. In all panels, black and blue lines show the observed values over all data and ICMEs removed, respectively, while red lines show values scaled for heliocentric distance. (a–c): Solar wind density. (d–f): Solar wind speed. (g–i): Heliospheric magnetic-field intensity.

around a 3% variation. As the solar wind density is expected to vary as $1/R^2$, we would therefore expect n_P to systematically vary by around 7%, if the solar wind were uniformly sampled. We therefore compute n_0, the density at a reference distance R_0, on the basis of n measured at some other distance R, using the following expression:

$$n_0 = n \frac{R^2}{R_0^2}. \tag{2}$$

We use $R_0 = 215 r_\odot$, the mean Earth–Sun distance. This R-scaled n_P is shown by the red lines in Figures 4a to c. While Figure 4a does appear to show a weak decline in n_P with R, and the scaled n_P does slightly reduce this, the variation is not explained by R alone. There are no obvious systematic variations of n_P with θ (Figures 4b and c), with or without scaling for R.

In order to scale the radial solar wind speed, V_r, for radial distance variations, we use the empirical solar wind acceleration expression from Riley and Lionello (2011):

$$V_0 = \frac{V}{1 + \alpha \left[1 - \exp(\frac{R_0 - R}{R_H}) \right]}, \tag{3}$$

where V is the measured solar wind speed at a distance R, V_0 is the scaled solar wind speed to a reference distance R_0, $\alpha = 0.15$ and $R_H = 50 r_\odot$. As seen in Figures 4d to f, this correction has little impact, due to the large R and the small ΔR considered here. It can be seen that the slight rising trend of V_r with R is not a direct result of solar wind acceleration over the heliocentric distances considered. There is no obvious trend in V_r with θ.

The magnetic-field magnitude, $|B|$, can be scaled for the R variation if an ideal Parker spiral (Parker, 1958) is assumed. In this approximation, the angle of the HMF to the radial direction, ϕ, at distance R in a constant solar wind speed V is given by:

$$\phi = \arctan \frac{\Omega R}{V}, \tag{4}$$

where Ω is the angular rotation speed of the Sun. The magnetic-field intensity, $|B|$, is therefore given by

$$|B| = \frac{B_r}{\cos \phi}, \tag{5}$$

where B_r is the radial magnetic field component at a distance R. By conservation of magnetic flux, this radial component, B_r, will fall off as $1/R^2$:

$$B_{r0} = B_r \frac{R^2}{R_0^2}, \tag{6}$$

where B_{r0} is the radial HMF intensity at a reference distance R_0. Thus the HMF intensity at a reference distance, R_0, can be estimated from:

$$|B|_0 = |B| \frac{R^2 \cos \phi}{R_0^2 \cos \phi_0}, \tag{7}$$

where ϕ_0 is the Parker spiral angle at a distance R_0.

Figure 4g shows that scaling $|B|$ for the R variation does reduce the observed trend of $|B|$ generally declining with R. This suggests that the observed decrease in $|B|$ with R is largely explained by the expected R variation. A weak apparent trend between $|B|$ and θ (Figure 4h) is also reduced when the variation with R is removed, suggesting an interplay between the orbital parameters R and θ.

4. Time-of-Year Variations

We now consider the variations in near-Earth solar wind properties over the year. Figures 5a to c show the n_P variations. The median value varies by around 25% over the year, reaching a minimum value around June ($F = 0.46$). This suggests the Earth's heliocentric distance variation could be the cause, as it reaches a maximum value at $F = 0.51$. However, while
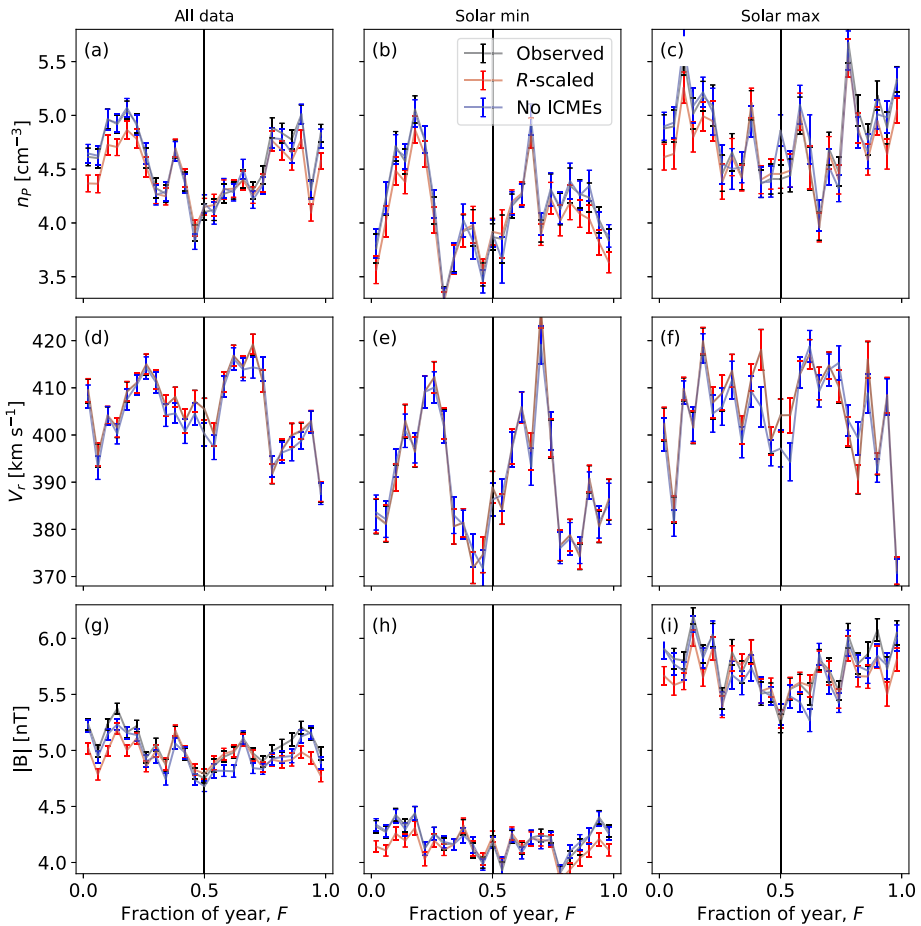
Figure 5 Variations of solar wind parameters with the time of year, F. Lines show median values, error bars are 95% confidence interval on the median. Black and blue show the observed values for all data and with ICMEs removed, respectively. Red lines show values scaled for heliocentric distance. (a–c): Solar wind density. (d–f): Solar wind radial speed. (g–i): Heliospheric magnetic-field intensity. Columns from left to right show all data, solar minimum, and solar maximum, respectively. For reference, $F = 0.5$ is shown as a solid vertical black line.

scaling the observations for the expected R variation does slightly decrease the n_P variation over the year, it does not produce the 25% variation that is observed. Furthermore, the n_P peaks are closer to the $|\theta|$ maxima in March and September than the R maximum in January, suggesting latitude – and hence systematic sampling of different solar wind types – may be contributing to the observed variation. Dividing the data by the solar activity level shows that the peaks are more prominent at solar minimum than maximum. At solar minimum, the timing of the density peaks is close, but not perfectly aligned, with the March and September $|\theta|$ peaks.

Figures 5d to f show the median V_r variation over the year. Particularly during solar minimum conditions, there is an obvious $|\theta|$ variation in the median V_r, with peaks in March and
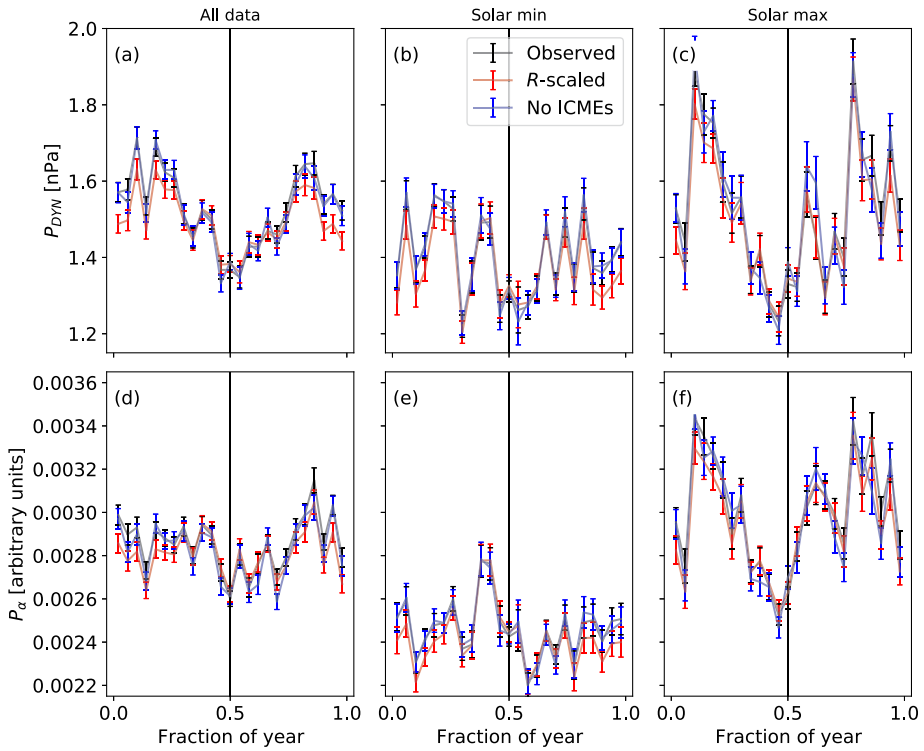
Figure 6   Variation in the solar wind dynamic pressure (P_{DYN}, top) and potential power input to the magnetosphere (P_α, bottom) with fraction of the year F. Lines show median values, error bars are 95% confidence interval on the median. Black and blue show the observed values for all data and with ICMEs removed, respectively. Red lines show values scaled for heliocentric distance. Columns from left to right show all data, solar minimum, and solar maximum, respectively. For reference, $F = 0.5$ is shown as a solid vertical black line.

September. This is about a $10 – 15\%$ variation. At solar maximum, there is some evidence of a similar variation present, though the data are generally less ordered at this time.

For $|B|$, there is also around a 5% variation over the year, peaking near the year start/end and reaching a minimum around July. This is most apparent at solar maximum. After adjusting the values for expected radial distance variation of an ideal Parker spiral, the $|B|$ variation with F is reduced.

Next, we investigate how n_P and V_r combine in the form of the solar wind dynamic pressure, $P_{DYN} = \rho V_r^2$, where ρ is the mass density of the solar wind. For simplicity, we use here only the proton number density, n_P, to compute ρ. Alpha particles, the next most abundant ion in the solar wind, only constitute a few percent of the solar wind by number, but their increased mass means they contribute around 10% to P_{DYN}. However, this value is approximately constant, as we find only small systematic variation of the alpha-to-proton ratio (not shown, but can be verified from the provided analysis code). Note that P_{DYN} is computed from hourly solar wind properties, not from the binned median values over the year.

Figures 6a to c show the resulting annual variations in dynamic pressure. Overall, there is about a 20% variation in P_{DYN} over the year. However, at solar maximum, this annual varia-

tion rises to around 60%. At both solar minimum and maximum, P_{DYN} reaches a minimum around $F = 0.5$ (June/July), when the Earth is farthest from the Sun. However, the peak in P_{DYN} in September suggests this is primarily due to sampling different types of solar wind, rather than an intrinsic distance effect. But the peak earlier in the year precedes the $|\theta|$ peak in March.

To estimate the potential contribution to the annual variation in geomagnetic activity, we use the Vasyliunas et al. (1982) solar wind-magnetosphere coupling function to estimate the potential power input of the solar wind to the magnetosphere, P_α:

$$P_\alpha = n^{(2/3-\alpha)} B^{(2\alpha)} V^{(7/3-2\alpha)} \sin^4(\theta_B/2), \qquad (8)$$

where α is an empirically-derived constant, found to be approximately 0.3 (Lockwood et al., 2017), and θ_B is the magnetic field clock angle in geocentric solar magnetic (GSM) coordinates. As we are not considering the annual variation in the orientation of Earth's magnetic field (i.e. the transformation from heliographic to Earth-centric coordinates), we set the $\sin^4(\theta_B/2)$ term to unity.

Figures 6d to f show the annual variation in P_α. Patterns are generally similar to P_{DYN}, owing to the common n_P and V_r factors and similar exponents. At solar maximum, there is around 30% annual variation in P_α, with peaks in mid February and September, again suggesting that preferential solar wind sampling by heliographic latitude is a significant contributing factor.

5. Conclusion

Geomagnetic activity exhibits many systematic trends over the day – as the Earth rotates – and over the year – as the Earth orbits the Sun. These variations are primarily driven by the geometric effects resulting from the changing orientation of Earth's magnetic field relative to that of the heliospheric magnetic field. However, there is an additional contribution to time-of-year variations in geomagnetic activity which is often overlooked. It is the changing position of the Earth within the heliosphere, specifically the heliocentric distance of the Earth from the Sun, and Earth's heliographic latitude. These two coupled variations mean the solar wind is not uniformly sampled through the year. The Sun-Earth distance varies between around 211 $r_\odot$ in January and 218 $r_\odot$ in July, while the heliographic latitude of Earth varies between $-7.25°$ in March and $7.25°$ in September. Using two solar cycles of ACE observations, we have demonstrated that there are systematic trends in the solar wind conditions encountered by Earth as a result.

The annual variation in solar wind speed closely follows the Earth's heliographic latitude, reaching peak values in March and September, and minima in June and November. It is most clearly seen at solar minimum, as expected (Owens et al., 2019, 2020), but is still also present at solar maximum. The amplitude of this variation is around 10 to 15%. However, the variation does seem to persist to the tail of the speed distribution; for example, at solar minimum, analysis of the solar wind speed probability distribution (not shown) suggests there is around 50% greater probability of encountering solar wind speeds in excess of 600 km s^{-1} during March and September than in June or December. This could potentially result in preferential energization of the radiation belts throughout the year (Reeves, Morley, and Cunningham, 2013). Similarly, while the occurrence of magnetospheric Kelvin-Helmholtz waves over the year appears to be primarily controlled by geometric effects such as the RM effect (Kavosi et al., 2023), the annual variation in solar wind speed may also contribute.

Annual variations are also present in the solar wind density, with an amplitude of around 25%. Perhaps surprisingly, this is unlikely to be the result of the Earth's heliocentric distance variation, which is expected to account for around a 7% variation over the year. The phase of the density variation is also inconsistent with heliocentric distance. Instead, it seems more closely related to the latitudinal variation of Earth and hence non-uniform sampling of the solar wind. Naively, we may expect the times of elevated solar wind speed to be associated with lower density, as fast coronal-hole wind is typically lower density than slower streamer-belt wind (e.g. Ebert et al., 2009). However, while this may be true for individual hours of data, in the time-averaged properties considered here, the annual variations of density and speed are not obviously anti-correlated. Indeed, if anything, there is some degree of correlation, with both speed and density reaching minima near the middle of the year and start/end of the year.

The magnetic field intensity shows a weaker annual trend, which is roughly consistent with Earth's heliocentric distance variation, peaking around January and reaching a low value around June/July.

The density and solar wind speed variations combine to give the dynamic pressure, P_{DYN} variation. However, despite the strong annual variations of the average speed and density at solar minimum, the resulting dynamic pressure variation is rather weak at this time. There is a minimum in P_{DYN} around June/July, and some suggestion of a maximum around September, but the amplitude is only 15%. This suggests that while the annual variations of density and speed are somewhat correlated, the individual hours of data that make up these average variations are somewhat anti-correlated, as might be expected from the properties of fast and slow wind. At solar maximum, the picture is quite different. The annual speed and density variations are less ordered at this time. But the individual hourly data combine to produce a strong P_{DYN} variation over the year. This peaks in mid-February and late-October, and reaches a minimum value in June/July. These dates are suggestive of the Earth's latitudinal variation, though not in complete agreement. The reason for such a timing offset is not known and could be insufficient sample size. The amplitude of the annual variation in P_{DYN} is around 60% at solar maximum. As the magnetopause distance at the nose scales by $P_{DYN}^{1/6}$, this would constitute about a 10%, or 1 Earth radius, variation. This too may have implications for the radiation belts, as magnetopause shadowing can cause particle loss (Staples et al., 2022).

Finally, we considered a proxy for geomagnetic activity, in the form of power input to the magnetosphere, P_α. The dominant factor in P_α is the angle between the heliospheric and magnetospheric magnetic fields. The variation of this orientation factor over the day and year has been well studied elsewhere (e.g. Lockwood et al., 2020b). Instead, we focus on the variation in the bulk properties, which determine the potential for geomagnetic activity for a given HMF orientation. The annual variation in P_α is qualitatively similar to that of P_{DYN}. At solar maximum, the potential power input to the magnetosphere seems to be more obviously modulated by heliographic latitude rather than heliocentric distance. The amplitude of the variation is around 30% at solar maximum, suggesting it could be a significant contribution to the overall annual variation in the base-level of geomagnetic activity.

Author contributions MO wrote the main manuscript. All authors involved in study design and reviewing manuscript.

Data Availability ACE data are available from cdaweb.gsfc.nasa.gov/pub/data/ace/magswe/level2_hdf/64sec. The updated Cane and Richardson near-Earth CME list is available from http://www.srl.caltech.edu/ACE/ASC/DATA/level3/icmetable2.htm. Sunspot data are provided by the Royal Observatory of Belgium SILSO and available from www.sidc.be/silso/DATA/SN_m_tot_V2.0.csv. HelioMAS data is available from https://www.predsci.com/mhdweb/home.php. All analysis and visualisation code is packaged with all required data here: www.github.com/University-of-Reading-Space-Science/AnnualVariations.

Declarations

Competing interests The authors declare no competing interests.

References

Bloch, T., Watt, C., Owens, M., McInnes, L., Macneil, A.R.: 2020, Data-driven classification of coronal hole and streamer belt solar wind. *Solar Phys.* **295**(3), 41. DOI.

Clette, F., Lefèvre, L.: 2016, The new sunspot number: assembling all corrections. *Solar Phys.* **291**, 2629. DOI.

Clette, F., Lefèvre, L., Chatzistergos, T., Hayakawa, H., Carrasco, V.M.S., Arlt, R., Cliver, E.W., Dudok de Wit, T., Friedli, T.K., Karachik, N., Kopp, G., Lockwood, M., Mathieu, S., Muñoz-Jaramillo, A., Owens, M., Pesnell, D., Pevtsov, A., Svalgaard, L., Usoskin, I.G., van Driel-Gesztelyi, L., Vaquero, J.M.: 2023, Recalibration of the sunspot-number: status report. *Solar Phys.* **298**(3), 44. DOI.

Cliver, E.W., Kamide, Y., Ling, A.G.: 2002, The semiannual variation of geomagnetic activity: phases and profiles for 130 years of aa data. *J. Atmos. Solar-Terr. Phys.* **64**(1), 47. DOI.

Cortie, A.L.: 1912, Sun-spots and terrestrial magnetic phenomena, 1898–1911: the cause of the annual variation in magnetic disturbances. *Mon. Not. Roy. Astron. Soc.* **73**(1), 52. DOI.

Cortie, A.L.: 1913, Sun-spots and terrestrial magnetic phenomena, 1898–1911: sun-spot areas, magnetic storms, and the sun's corona (Third paper.). *Mon. Not. Roy. Astron. Soc.* **73**(6), 431. DOI.

Dungey, J.W.: 1961, Interplanetary magnetic field and the auroral zones. *Phys. Rev. Lett.* **6**, 47. DOI.

Ebert, R.W., McComas, D.J., Elliott, H.A., Forsyth, R.J., Gosling, J.T.: 2009, Bulk properties of the slow and fast solar wind and interplanetary coronal mass ejections measured by Ulysses: Three polar orbits of observations. *J. Geophys. Res.* **114**(A1). DOI.

Gosling, J.T.: 1993, The solar flare myth. *J. Geophys. Res.* **98**, 18937. DOI.

Kavosi, S., Raeder, J., Johnson, J.R., Nykyri, K., Farrugia, C.J.: 2023, Seasonal and diurnal variations of Kelvin-Helmholtz instability at terrestrial magnetopause. *Nat. Commun.* **14**(1), 2513. DOI.

Lockwood, M., Milan, S.E.: 2023, Universal Time variations in the magnetosphere. *Front. Astron. Space Sci.* **10**. DOI.

Lockwood, M., Owens, M.J., Barnard, L.A., Bentley, S., Scott, C.J., Watt, C.E.: 2016, On the origins and timescales of geoeffective IMF. *Space Weather* **14**(6), 406. DOI.

Lockwood, M., Owens, M.J., Barnard, L.A., Scott, C.J., Watt, C.E.: 2017, Space climate and space weather over the past 400 years: 1. The power input to the magnetosphere. *J. Space Weather Space Clim.* **7**, A25. DOI.

Lockwood, M., Chambodut, A., Finch, I.D., Barnard, L.A., Owens, M.J., Haines, C.: 2019, Time-of-day/time-of-year response functions of planetary geomagnetic indices. *J. Space Weather Space Clim.* **9**, A20. DOI.

Lockwood, M., McWilliams, K.A., Owens, M.J., Barnard, L.A., Watt, C.E., Scott, C.J., Macneil, A.R., Coxon, J.C.: 2020b, Semi-annual, annual and universal time variations in the magnetosphere and in geomagnetic activity: 2. Response to solar wind power input and relationships with solar wind dynamic pressure and magnetospheric flux transport. *J. Space Weather Space Clim.* **10**, 30. DOI.

Lockwood, M., Owens, M.J., Barnard, L.A., Haines, C., Scott, C.J., McWilliams, K.A., Coxon, J.C.: 2020a, Semi-annual, annual and universal time variations in the magnetosphere and in geomagnetic activity: 1. Geomagnetic data. *J. Space Weather Space Clim.* **10**, 23. DOI.

McComas, D.J., Bame, S.J., Barker, S.J., Feldman, W.C., Phillips, J.L., Riley, P., Griffee, J.W.: 1998, Solar wind electron proton alpha monitor (SWEPAM) for the advanced composition explorer. *Space Sci. Rev.* **86**, 563. DOI.

McComas, D.J., Elliott, H.A., Schwadron, N.A., Gosling, J.T., Skoug, R.M., Goldstein, B.E.: 2003, The three-dimensional solar wind around solar maximum. *Geophys. Res. Lett.* 30. DOI.

McGill, R., Tukey, J.W., Larsen, W.A.: 1978, Variations of box plots. *Am. Stat.* **32**(1), 12. DOI.

McIntosh, D.H., Feather, N.: 1959, On the annual variation of magnetic disturbance. *Phil. Trans. Roy. Soc. London* **251**(1001), 525. DOI.

Murayama, T.: 1974, Origin of the semiannual variation of geomagnetic Kp indices. *J. Geophys. Res.* **79**(1), 297. DOI.

Orlando, M., Moreno, G., Parisi, M., Storini, M.: 1993, Semiannual variation of the geomagnetic activity and solar wind parameters. *Geophys. Res. Lett.* **20**(20), 2271. DOI.

Owens, M.: 2020, Solar-wind structure. In: *Oxford Research Encyclopedia of Physics*. DOI.

Owens, M.J., Riley, P., Lang, M., Lockwood, M.: 2019, Near-Earth solar wind forecasting using corotation from L5: the error introduced by heliographic latitude offset. *Space Weather* **17**, 1105. DOI.

Owens, M.J., Lang, M., Riley, P., Lockwood, M., Lawless, A.S.: 2020, Quantifying the latitudinal representivity of in situ solar wind observations. *J. Space Weather Space Clim.* **10**, 8. DOI.

Owens, M.J., Chakraborty, N., Turner, H., Lang, M., Riley, P., Lockwood, M., Barnard, L.A., Chi, Y.: 2022, Rate of change of large-scale solar-wind structure. *Solar Phys.* **297**(7), 83. DOI.

Parker, E.N.: 1958, Dynamics of the interplanetary gas and magnetic fields. *Astrophys. J.* **128**, 664. DOI.

Reeves, G., Morley, S., Cunningham, G.: 2013, Long-term variations in solar wind velocity and radiation belt electrons. *J. Geophys. Res.* **118**(3), 1040. DOI.

Richardson, I.G., Cane, H.V.: 2010, Near-Earth interplanetary coronal mass ejections during solar Cycle 23 (1996 – 2009): catalog and summary of properties. *Solar Phys.* **264**(1), 189. DOI.

Riley, P., Lionello, R.: 2011, Mapping solar wind streams from the sun to 1 AU: a comparison of techniques. *Solar Phys.* **270**(2), 575. DOI.

Rosenberg, R.L., Coleman, P.J.: 1969, Heliographic latitude dependence of the dominant polarity of the interplanetary magnetic field. *J. Geophys. Res.* **74**(24), 5611. DOI.

Russell, C.T., McPherron, R.L.: 1973, Semiannual variation of geomagnetic activity. *J. Geophys. Res.* **78**(1), 92. DOI.

Smith, C.W., L'Heureux, J., Ness, N.F., Acuna, M.H., Burlaga, L.F., Scheifele, J.: 1998, The ACE magnetic fields experiment. *Space Sci. Rev.* **86**, 613. DOI.

Staples, F.A., Kellerman, A., Murphy, K.R., Rae, I.J., Sandhu, J.K., Forsyth, C.: 2022, Resolving magnetopause shadowing using multimission measurements of phase space density. *J. Geophys. Res.* 127(2). DOI.

Vasyliunas, V.M., Kan, J.R., Siscoe, G.L., Akasofu, S.-I.: 1982, Scaling relations governing magnetospheric energy transfer. *Planet. Space Sci.* **30**(4), 359. DOI.

Zhao, H., Zong, Q.-G.: 2012, Seasonal and diurnal variation of geomagnetic activity: Russell-McPherron effect during different IMF polarity and/or extreme solar wind conditions. *J. Geophys. Res.* 117(A11). DOI.